

MSCDA: Multi-level Semantic-guided Contrast Improves Unsupervised Domain Adaptation for Breast MRI Segmentation in Small Datasets

Sheng Kuang^a, Henry C. Woodruff^{a,b}, Renee Granzier^c, Thiemo J.A. van Nijnen^{b,d}, Marc B.I. Lobbes^{b,d,e}, Marjolein L. Smidt^{c,d}, Philippe Lambin^{a,b}, Siamak Mehrkanoon^{f,*}

^a*The D-Lab, Department of Precision Medicine, GROW – School of Oncology and Reproduction, Maastricht University, Maastricht, The Netherlands*

^b*Department of Radiology and Nuclear Medicine, Maastricht University Medical Centre+, Maastricht, The Netherlands*

^c*Department of Surgery, Maastricht University Medical Centre+, Maastricht, The Netherlands*

^d*GROW – School for Oncology and Reproduction, Maastricht University, Maastricht, The Netherlands*

^e*Department of Medical Imaging, Zuyderland Medical Center, Sittard-Geleen, The Netherlands*

^f*Department of Information and Computing Sciences, Utrecht University, Utrecht, The Netherlands*

Abstract

Deep learning (DL) applied to breast tissue segmentation in magnetic resonance imaging (MRI) has received increased attention in the last decade, however, the domain shift which arises from different vendors, acquisition protocols, and biological heterogeneity, remains an important but challenging obstacle on the path towards clinical implementation. Recently, unsupervised domain adaptation (UDA) methods have attempted to mitigate this problem by incorporating self-training with contrastive learning. To better exploit the underlying semantic information of the image at different levels, we propose a Multi-level Semantic-guided Contrastive Domain Adaptation (MSCDA) framework to align the feature representation between domains. In particular, we extend the contrastive loss by incorporating pixel-to-pixel, pixel-to-centroid, and centroid-to-centroid contrasts to integrate semantic information of images. We utilize a category-wise cross-domain sampling strategy to sample anchors from target images and build a hybrid memory bank to store samples from source images. Two breast MRI datasets were retrospectively collected: The source dataset contains non-contrast MRI examinations from 11 healthy volunteers and the target dataset contains contrast-enhanced MRI examinations of 134 invasive breast cancer patients. We set up experiments from source T2W image to target dynamic contrast-enhanced (DCE)-T1W image (T2W-to-T1W) and from source T1W image to target T2W image (T1W-to-T2W). The proposed method achieved Dice similarity coefficient (DSC) of 89.2% and 84.0% in T2W-to-T1W and T1W-to-T2W, respectively, outperforming state-of-the-art methods. Notably, good performance is still achieved with a smaller source dataset, proving that our framework is label-efficient.

Keywords: Breast segmentation, Unsupervised domain adaptation, Contrastive learning

1. Introduction

Breast cancer is the most commonly diagnosed cancer in women and contributes to 15% of mortality worldwide, ranking as a leading cause of death in many countries (Francies et al. (2020); Sung et al. (2021)). The significantly increasing mortality rates of breast cancer, especially in developing countries and low-income regions, lead to increased burdens for patients, their families, and society, highlighting the need for early detection and intervention (Azamjah et al. (2019)). In the past decades, breast magnetic resonance imaging (MRI) has been recommended to supplement conventional mammography and ultrasound techniques to screen women at a high risk of breast cancer and determine the extent of breast cancer after diagnosis (Saslow et al. (2007); Gupta and Billadello (2017)).

A further step towards advanced MRI-based diagnosis is accurate breast segmentation. In clinical routine, whole-breast segmentation and analysis are conducted manually relying on the expertise of clinicians, which is a challenging and time-consuming process. With the advent of computer vision, atlas- and statistical-based methods with high accuracy compared to manual segmentation have been proposed (Wu et al. (2013)). Recently, numerous deep learning (DL) approaches have been developed to further improve the performance of breast segmentation. These tools extract salient features directly from the images and automatically segment the breast boundary (Dalmış et al. (2017); Hu et al. (2018); Ivanovska et al. (2019)), breast fibroglandular tissue (FGT) (Dalmış et al. (2017); Ivanovska et al. (2019)) and breast lesions (Zhang et al. (2018b); Gallego-Ortiz and Martel (2017); Negi et al. (2020)), which are less prone to errors and have achieved encouraging Dice similarity coefficients (DSCs) in various datasets.

*Corresponding author

Email address: s.mehrkanoon@uu.nl (Siamak Mehrkanoon)

Despite the high popularity of DL approaches, there are some barriers on the path to clinical implementation. One main concern is performance degradation due to large inhomogeneities present in MRI datasets, leading to differing imaging feature distributions between training (source domain) and testing (target domain) datasets, also known as the domain shift problem. For instance, most available imaging datasets from different medical centers are acquired with different acquisition parameters, protocols and hardware vendors (Perone et al. (2019)). Moreover, patient heterogeneity, stemming from different breast sizes, menstrual cycle effects and stage of disease progression, leads to inconsistencies within the images, which may result in unstable performance of DL models (Granzier et al. (2022)). Although this problem could be addressed by acquiring large and varied datasets of accurately annotated target images for training, this exercise would be labor-consuming and expensive, and is further hindered by legal and ethical considerations regarding the sharing of patient data. Thus, recent published studies (Hoffman et al. (2018); Hoyer et al. (2022); Hoffman et al. (2016)) focus on developing unsupervised domain adaptation (UDA) methods to mitigate the distribution discrepancy without target labels.

Recent advances in UDA methods have enabled its application to medical images by transferring the knowledge from the source domain to the target domain (Perone et al. (2019); Shantis et al. (2019); Liu et al. (2022); Chaitanya et al. (2020)). For instance, adversarial learning (e.g. Cycle-GAN) adopts the discriminator to align the distribution in the latent feature space (Dou et al. (2018); Hoffman et al. (2018)) or label space (Tsai et al. (2018)). In practice, these methods suffer from training instability and model collapse (Zhu et al. (2017)). Self-training (Tarpainen and Valpola (2017); Perone et al. (2019)) is another promising method which combines entropy minimizing (Vu et al. (2019)), pseudo-label denoising (Zhang et al. (2021)), adversarial learning (Shantis et al. (2019)), generative methods (Zhao et al. (2021b)) or contrastive learning (Zhang et al. (2022); Liu et al. (2022); Chaitanya et al. (2020)). More recently, incorporating self-training with complementary contrastive learning shows remarkable performance improvement by utilizing the ground truth and pseudo labels as supervised semantic signals to guide the training.

Contrastive learning in this case explicitly computes the inter-category similarity between pixel representation pairs (Liu et al. (2022)) (refers to pixel-to-pixel (P2P) contrast) aiming to learn an invariant representation in feature space. However, it still suffers from the following two major concerns that are not taken into account: (i) P2P contrast skips the structure context of adjacent pixels, so it does not extensively exploit the semantic information present in the MRI scan. To alleviate this problem, we propose a method to integrate different levels of semantic information into a contrastive loss function. More specifically, the mean value of the pixel representations of a specific category, i.e., the centroid, should be similar to the pixels contained in the region. Likewise, centroids, regardless of whether they are from the same domain, should also be close to centroids of the same category and far away from centroids of other categories. We denote these two relations as pixel-to-

centroid (P2C) and centroid-to-centroid (C2C) respectively. (ii) A common practice to perform inter-category contrast is to generate positive and negative pairs by sampling partial pixel representations in a mini-batch (Chaitanya et al. (2020)). However, the imbalanced proportion between background and regions of interest (ROIs) in the breast MRIs poses a challenge to obtain adequate pairs during training. To address this problem, we build a hybrid memory bank and optimize the sampling strategy to ensure enough cross-domain positive and negative pairs especially for the highly imbalanced mini-batches. Additionally, we also explore the impact of anchors and samples from different domains on model performance.

In summary, we extend the contrastive UDA framework for breast segmentation to further mitigate the domain shift problem. To the best of our knowledge, this is the first attempt to apply contrastive UDA in breast MRI. We briefly provide the novel contributions of our work as follows:

1. To solve the domain shift problem in breast MRI, we develop a novel Multi-level Semantic-guided Contrastive Domain Adaptation (MSCDA) framework for cross-domain breast tissue segmentation.
2. To exploit the semantic information present in source labels, we propose a method that combines pixel-to-pixel, pixel-to-centroid and centroid-to-centroid contrasts into the loss function.
3. To resolve the data imbalance problem, we develop a hybrid memory bank that saves both category-wise pixel and centroid samples. We further investigate a category-wise cross-domain sampling strategy to form adequate contrastive pairs.
4. To validate the performance of the UDA framework, we replicate our experiment under multiple source datasets of different sizes. The results show robust performance and label-efficient learning ability. We further show that our framework achieves comparable performance to supervised learning.

2. Related Works

2.1. Semantic Segmentation

Semantic segmentation is an essential and hot topic in computer vision, achieving automatic categorization of each pixel (or voxel) into one or more categories. In recent years, convolutional neural networks (CNNs) have shown significant results in multiple fields. Fully convolutional network (FCN) (Long et al. (2015)), as one of the most remarkable early-stage segmentation architectures, demonstrated the pixel-level representation learning ability of CNNs. However, CNNs are still far from maturity in terms of accuracy and efficiency. Therefore, many mechanisms have been proposed to improve segmentation performance. For instance, U-Net Ronneberger et al. (2015) introduced skip connections in an encoder-decoder design to solve the vanishing gradient problem; DeepLab v3+ (Chen et al. (2018)) proposed Atrous Spatial Pyramid Pooling (ASPP) to capture more context information in multi-scale

receptive fields. Meanwhile, inspired by the effectiveness of residual blocks, ResNet (He et al. (2016)) was adopted as the backbone in many encoder-decoder segmentation frameworks (Chen et al. (2018); Wu et al. (2019); Zhang et al. (2018a); He et al. (2019)) to provide deep feature representations.

DL techniques have also been widely adopted in the field of medical imaging that pave the way towards more precise and automated clinical diagnosis and prognosis. Common DL methods focus on the segmentation of contours (Zhang et al. (2020); Dalmış et al. (2017); Zhang et al. (2019); Piantadosi et al. (2018)) and lesions (Dalmış et al. (2017); Zhang et al. (2018c); El Adoui et al. (2019)) in breast magnetic resonance imaging (MRI). Despite the promising performance, these methods require large datasets with expert annotations, expensive and hard to realize the current data-sharing paradigm.

2.2. Contrastive Learning

Contrastive learning (CL) was introduced as a self-supervised learning framework, allowing the model to learn representations without labels (Oord et al. (2018); He et al. (2020); Chen et al. (2020b,a); Grill et al. (2020)). An essential step of early CL methods is to build a pretext task, such as instance discrimination (Wu et al. (2018); He et al. (2020); Chen et al. (2020a)), to discriminate a positive pair (two augmented views of an identical image) from negative pairs (augmented view of other images). Based on this pioneering approach, many subsequent advanced mechanisms have been proposed to improve the representation learning ability. For example, Moco v1 (He et al. (2020)) and v2 (Chen et al. (2020b)) combined a momentum encoder with a first-in-first-out queue to maintain more negative samples. This results in an improved classification performance e.g., ImageNet (Deng et al. (2009)) and enables training the network on normal graphics processing units (GPUs). Afterwards, the projection head (Chen et al. (2020a)) and the prediction head (Grill et al. (2020)) were introduced respectively to improve the classification accuracy on downstream tasks.

For semantic segmentation tasks, recent CL works leverage the pixel-level labels as supervised signals (Zhao et al. (2021a); Zhong et al. (2021); Hu et al. (2021); Wang et al. (2021); Chaitanya et al. (2020)). The underlying idea is to group the pixel representations from the same category and to separate pixel representations from different categories. Zhao et al. (2021a) introduced a label-efficient two-stage method that pre-trained the network by using P2P contrastive loss and then fine-tuned the network using cross-entropy (CE) loss (Bishop and Nasrabadi (2006)). PC²Seg (Zhong et al. (2021)) improved this method in a one-stage semi-supervised learning (SSL) approach by jointly updating the network weights with pixel contrastive loss and consistency loss. ContrastiveSeg (Wang et al. (2021)) combined pixel-to-region contrastive loss to explicitly leverage the context relation across images. Similar to Zhong et al. (2021); Wang et al. (2021), the authors in Chaitanya et al. (2020) validated the effectiveness of different sampling strategies on contrastive learning for multiple medical MRI segmentation tasks (Bernard et al. (2018); Antonelli et al. (2022); Zhuang and Shen (2016)).

2.3. Unsupervised Domain Adaptation

Unsupervised Domain Adaptation (UDA) is used to generalize learned knowledge from a labeled source domain to an unlabeled target domain. The key challenge of UDA is domain shift, i.e., the inconsistent data distribution across domains, which usually causes performance degradation of models. Early machine learning methods utilized different feature transformations or regularizations to overcome this problem (Kouw and Loog (2018); Mehrkanoon and Suykens (2017); Mehrkanoon (2019)).

A number of existing DL methods solve the domain shift problem using adversarial learning or self-training-based approaches. Adversarial learning utilizes generative adversarial networks (GANs) (Goodfellow et al. (2014)) to align the distribution of the feature space (Tzeng et al. (2017); Hoffman et al. (2016); Chen et al. (2019b); Dou et al. (2018)) or label space (Vu et al. (2019); Dou et al. (2018); Tsai et al. (2018)). In particular, CycleGAN (Zhu et al. (2017); Kim et al. (2017); Yi et al. (2017)) has been extensively explored and adopted in medical image UDA (Jiang et al. (2018); Zhang et al. (2018d); Chen et al. (2019a); Guan and Liu (2021)) because of its ability to translate the ‘style’ of the source domain to the target domain in an unpaired way.

Self-training, frequently used in SSL, uses the predictions of the target domain as pseudo-labels and retrains the model iteratively. A typical self-training network (Tarpainen and Valpola (2017)) generates pseudo-labels from a momentum teacher network and distills knowledge to the student network by using the consistency loss. The authors in Perone et al. (2019); Perone and Cohen-Adad (2018) improved the self-training method by aligning the geometrical transformation between the student and teacher networks. DART (Shanis et al. (2019)) and MT-UDA (Zhao et al. (2021b)) combined self-training with adversarial learning in different ways, both receiving promising results. For imbalanced datasets, different denoising methods and sampling strategies have been proposed to improve the quality of pseudo-labels (Zhang et al. (2021); Hoyer et al. (2022); Xie et al. (2022)). Similar to Chaitanya et al. (2020), recent self-training approaches (Xie et al. (2022); Zhang et al. (2022)) incorporated CL, i.e. unsupervised contrastive domain adaptation, to align cross-domain features by sampling or merging contrastive feature embeddings across categories. In this study, we integrate three kinds of contrastive losses and a category-wise cross-domain sampling strategy to accomplish the UDA segmentation task for breast MRI.

3. Method

3.1. Problem Definition

Source domain data and target domain data are two sets of data used in the domain adaptation problem. The source domain data $X_s = \{x_s\}_{i=1}^M$ have pixel-level labels whereas the target domain image data $X_t = \{x_t\}_{i=1}^N$ are unlabeled. We aim at developing a method that can learn from the labeled source domain and be applied to the target domain. In particular, the learned

Table 1: Important notations in our proposed method.

| Notations | Description |
|----------------------------|--------------------------------------------------------------------------------------------------------------|
| x_s, x_t, y_s, \hat{y}_s | Source image, target image, source image ground truth and corresponding one-hot representation respectively; |
| p_s, p_t | Student network probability map of the source and target images respectively; |
| p'_s, p'_t | Teacher network probability map of the source and target images respectively; |
| z_t | Student network feature embedding of the target image; |
| z'_s | Teacher network feature embedding of the source image; |
| \hat{y}_t, \hat{y}'_t | One-hot pseudo-label of p_t and p'_t respectively ($y = \text{argmax}(p)$); |
| v_s^k, v_t^k | Pixel feature embedding of category k of the source and target images respectively; |
| c_s^k, c_t^k | Centroid feature embedding of category k of the source and target images respectively; |
| $Q_{pixel}, Q_{centroid}$ | Pixel queue and centroid queue in the memory bank. |

network is used to classify each pixel of the target domain image into K categories. A direct approach is to train the network in a supervised manner on the source domain and apply it directly to the target domain. However, the performance of the network often drops because of the aforementioned domain gap between source and target domains. To address this concern, we propose a new domain adaptation approach, named MSCDA, based on the combination of self-training and contrastive learning.

3.2. Overall Framework

The proposed domain adaptation framework is depicted in Fig. 1. It consists of a student network and a momentum teacher network. The student network consists of four main components, a feature encoder f_e , a feature decoder f_d , a projection head f_{proj} , and an additional prediction head f_{pred} . These components are correspondingly mapped in the teacher network with the only exception of the last component (i.e., the prediction head). The three components in the teacher network are called f'_e , f'_d and f'_{pred} . The important notations are listed in Table 1.

In the student network, the feature encoder f_e maps the input MRI image $x \in \mathbb{R}^{H \times W \times 1}$ into a high dimension feature map $h \in \mathbb{R}^{H' \times W' \times C}$. Next, h is transferred into a segmentation probability map $p \in \mathbb{R}^{H \times W \times K}$ and a low dimension feature embedding $z \in \mathbb{R}^{H' \times W' \times D}$ through two forward passes, hereafter referred to as segmentation and contrast paths, respectively. In the first forward pass (segmentation path), the decoder f_d generates the segmentation probability map p of the input h . In the second forward pass (contrast path), the projection head f_{proj} and prediction head f_{pred} jointly reduce the feature map into a low-dimension projected feature embedding $z = f_{pred}(f_{proj}(h))$. Similar steps are conducted in the teacher network, yielding the momentum probability map p' and feature embedding z' . Finally, the probability map p and p' are used for self-training

while the projected feature embeddings z and z' are used for semantic-guided contrastive learning to diminish the discrepancy between the two domains. The overall loss function is given by:

$$\mathcal{L} = \mathcal{L}_{seg} + \lambda_1 \mathcal{L}_{con} + \lambda_2 \mathcal{L}_{ctr}, \quad (1)$$

where \mathcal{L}_{seg} is the supervised segmentation loss, \mathcal{L}_{con} is the consistency loss, \mathcal{L}_{ctr} is the contrastive loss, and λ_1 and λ_2 are the regularization parameters of the corresponding losses. The summation of segmentation and consistency loss is henceforth referred to as the self-training loss. We elaborate the self-training loss in Section 3.3 and our proposed contrastive loss in Section 3.4.

3.3. Self-training

Following the self-training paradigm (Perone et al. (2019)), two optimization goals were established. The first goal is to perform supervised learning on the student network from source image labels. The second goal is that the student network learns the pseudo labels generated by the teacher network to distill knowledge from target images. Only the weights in the segmentation path of both networks are updated in this phase.

3.3.1. Supervised Learning

In supervised learning, we employ a hybrid segmentation loss (Isensee et al. (2018)) that combines Dice loss (Sudre et al. (2017)) and CE loss, and is formulated as:

$$\mathcal{L}_{seg} = \frac{1}{2} \mathcal{L}_{Dice}(p_s, \hat{y}_s) + \frac{1}{2} \mathcal{L}_{ce}(p_s, \hat{y}_s), \quad (2)$$

where \hat{y}_s is the one-hot ground truth and p_s is the probability map of the source domain image in the student network.

3.3.2. Distilling Knowledge from Pseudo Labels

The pseudo label of the target image is generated by the segmentation path in the momentum teacher network iteratively:

$$\hat{y}'_t = \text{argmax}(p'_t), \quad (3)$$

where p'_t is the probability map of the target domain image in the teacher network. In order to distill knowledge from the pseudo label, an extra consistency loss is added between the two networks. In other words, the target image segmentation p_t generated by the student network is guided by the pseudo label \hat{y}'_t . The consistency loss is formulated as:

$$\mathcal{L}_{con} = \frac{1}{H \times W \times K} \sum_{i=1}^{H \times W} \sum_{k=1}^{K-1} \|p_t^{(i,k)} - \hat{y}'_t^{(i,k)}\|^2, \quad (4)$$

where i is the pixel index of the image and k is the category. Here, we update the weights of the student network by means of back propagation. However, in the teacher network, a stop-gradient operation is applied, and the network weights are updated by exponential moving average (EMA):

$$\Theta' \leftarrow \alpha \Theta' + (1 - \alpha) \Theta, \quad (5)$$

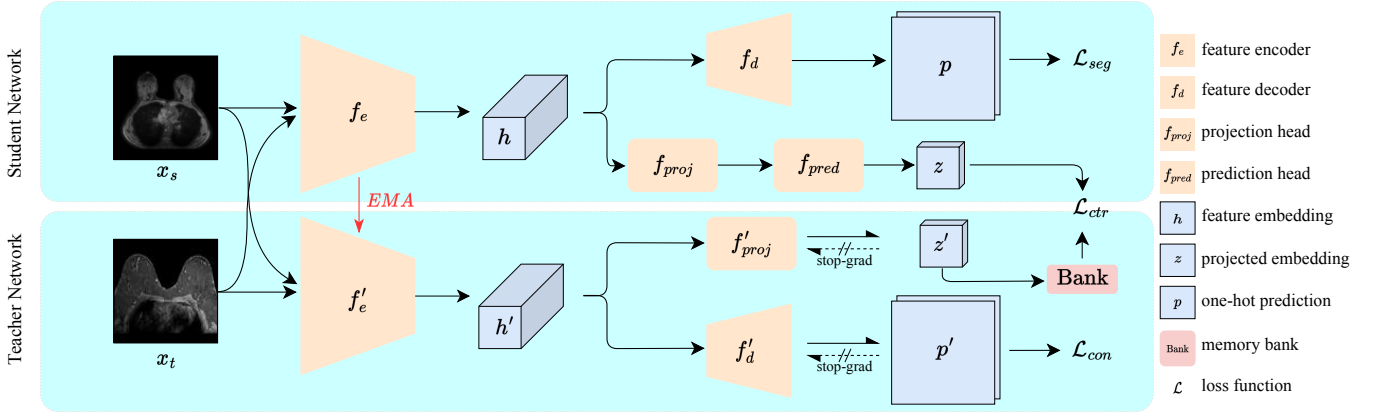


Figure 1: The proposed framework of the unsupervised domain adaptation method, named MSCDA. A source image x_s and a target image x_t are the inputs to the student network and the momentum teacher networks, respectively. Each network consists of a segmentation path and a contrast path. The student network is trained by a supervised segmentation loss, an inter-network consistency loss and a multi-level contrastive loss. The teacher network updates the weights by exponential moving average (EMA). The training procedure is layer out in Sections 3.3 and 3.4.

where Θ and Θ' are the weights of the student network and teacher network respectively, and $\alpha \in (0, 1)$ is the momentum coefficient.

Combining data augmentation with self-training has been shown to improve the domain adaptation performance (Tartinen and Valpola (2017); Chen et al. (2020a)). The student network receives strongly-augmented images, and the teacher network receives weakly-augmented images during the training process. Random resized cropping is used as the weak augmentation method, and random brightness, contrast and Gaussian blur are used as strong augmentation methods. The strongly-augmented path learns a robust feature representation from the weakly-augmented path that has less disruption.

3.4. Semantic-guided Contrastive Loss

In order to improve the performance of our UDA framework even further, we incorporate a multi-level semantic-guided contrast to the self-training framework. The idea is to leverage the ground truth of the source domain as supervised signals to enforce the encoder to learn a well-aligned feature representation that mitigates the domain discrepancy. A common way is to categorize the feature embedding and conduct contrastive learning using the pixels or centroids between domains. In our approach, we develop the contrastive loss at P2P, P2C and C2C levels to directly utilize multi-level semantic information to guide the feature alignment. The data flow of our proposed contrastive loss is depicted in Fig. 2.

3.4.1. Preliminaries

In unsupervised contrastive segmentation approaches, the contrast is performed using a randomly selected sample (called the anchor) v , a positive sample v^+ and n negative samples $V^- = \{v_1^-, v_2^-, \dots, v_n^-\}$. The aim is to learn a feature representation that yields high similarity in positive pairs (v, v^+) and low similarity in negative pairs (v, v^-) . Following He et al. (2020); Chen et al. (2020b); Zhong et al. (2021), we utilize the InfoNCE as

our loss function, which is given as follows:

$$\mathcal{L}_{ctr} = -\log \frac{\exp(v \cdot v^+ / \tau)}{\exp(v \cdot v^+ / \tau) + \sum_{i=1}^n \exp(v \cdot v_i^- / \tau)}, \quad (6)$$

where n is the number of negative samples per anchor, ‘ \cdot ’ is the dot product between two samples, and τ is a temperature hyperparameter that controls the gradient penalty of hard negative samples, which is empirically set to 0.07 (He et al. (2020)). Here, samples are selected from D -dimensional feature embedding followed by l_2 -normalization.

3.4.2. Feature Categorization

Feature categorization is a necessary step required for supervised contrastive learning in the feature space. To utilize the semantic information effectively, we categorize the feature embedding from both domains. For the source image, the feature embedding in the teacher network and its ground truth are required. Given the l_2 -normalized target network feature embedding of a source image $z'_s \in \mathbb{R}^{H' \times W' \times D}$ and the one-hot ground truth $\hat{y}_s \in \mathbb{R}^{H \times W \times K}$, we first down-sample the one-hot ground truth into $\bar{y}_s \in \mathbb{R}^{H' \times W' \times K}$ to fit the embedding size, then assign the category label index $k \in \{0, K-1\}$ of \bar{y}_s to each pixel of z'_s (Fig. 2(a)). Similarly, the target image embedding z_t can also be categorized using the pseudo label \hat{y}_t . Based on the categorized feature embedding, we further compute the category-wise mean value of pixels of the feature embedding as the centroid $C = \{c^k\}_{k=0}^{K-1}$, which is given as follows:

$$c^k = \frac{1}{|\mathbb{Y}^k|} \sum_{i=1}^{H' \times W'} \mathbb{1}[\bar{y}^{(i,k)} = k] \cdot z^i, \quad (7)$$

where $\mathbb{1}[\cdot]$ is an indicator function that returns 1 when the condition holds and 0 otherwise, z^i is the i^{th} pixel of the feature embedding and $\bar{y}^{(i,k)}$ is the down-sampled label which belongs to the i^{th} pixel and category k , \mathbb{Y}^k is the set of labels of category k .

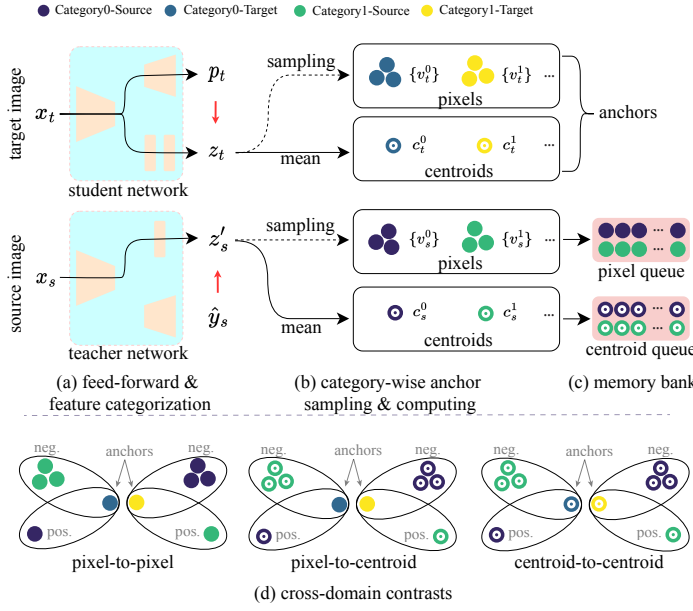


Figure 2: The data flow of our proposed multi-level contrastive loss. (a) feed-forward and feature categorization. (b) category-wise anchor sampling and computing. (c) memory bank. (d) proposed multi-level cross-domain contrasts.

3.4.3. Memory Bank & Sampling Strategy

Although the number of negative samples is critical for learning the feature representation (He et al. (2020)), insufficient negative pairs of each batch in the breast MRI segmentation task may occur because of the highly imbalanced ration between foreground and background pixels. To overcome this problem, we utilize two category-wise queues as a memory bank to maintain the pixel and centroid samples from the **source** images in the **teacher** network. However, keeping all pixels in the queue is not feasible because of GPU memory limitations. Thus, we uniformly sample b pixels from each category in the feature embedding to the pixel queue (Fig. 2(b,c)). This under-sampling strategy enables the queue to maintain enough balanced, but not redundant, pixel samples. The pixel queue Q_{pixel} and the centroid queue $Q_{centroid}$ can be represented as:

$$Q_{pixel} = \{Q_{pixel}^k\}_{k=0}^{K-1}, \quad Q_{pixel}^k = \{v_{(s,i)}^k\}_{i=1}^{B_p}, \quad (8)$$

$$Q_{centroid} = \{Q_{centroid}^k\}_{k=0}^{K-1}, \quad Q_{centroid}^k = \{c_{(s,i)}^k\}_{i=1}^{B_c}, \quad (9)$$

where Q_{pixel}^k is the pixel queue of category k , $v_{(s,i)}^k$ is the i^{th} source pixel sample of category k , $Q_{centroid}^k$ is the centroid queue of category k , $c_{(s,i)}^k$ is the i^{th} source centroid sample of category k , and B_p and B_c are the size of the queue respectively.

3.4.4. Pixel-to-pixel Contrast

We perform the pixel-to-pixel (P2P) contrastive loss to align the cross-domain feature representation of the same category. To resolve this problem, we first sample m anchors from each category of the **target** feature embedding z_t in the **student** network, denoted as set V_t^k . Then, for each anchor $v_t^k \in V_t^k$ with category label k , we sample a **source** pixel of the same category

from the pixel queue Q_{pixel} to form a positive pair (v_t^k, v_s^{k+}) , and sample n **source** pixels of category $q \in \mathbb{K} \setminus \{k\}$ to form n negative pairs (v_t^k, v_s^{q-}) . Based on these positive and negative pairs, the InfoNCE loss of a single **target** anchor is computed by using Eq.(6). Overall, the P2P loss is defined as:

$$\mathcal{L}_{ctr}^{P2P} = \frac{1}{\sum_{k=0}^{K-1} |V_t^k|} \sum_{k=0}^{K-1} \sum_{v_t^k \in V_t^k} \mathcal{L}_{ctr}(v_t^k, v_s^{k+}, V_s^{q-}), \quad (10)$$

where $|\cdot|$ is the number of elements in a set, and V_s^{q-} is the set of negative source pixels. Note that the number of pixels labeled as foreground categories might be less than m (or even 0) if the model predicts a few (or no) breast tissue labels in a mini-batch. Nevertheless, benefiting from the category-wise memory bank, the contrast loss can still be computed even if all pixels in a mini-batch belong to the same category.

3.4.5. Pixel-to-centroid Contrast

Due to the under-sampling strategy in selecting anchors and updating the memory bank, the network may suffer from inadequate semantic knowledge and thereby be difficult to converge. This issue is further addressed by incorporating P2C and C2C contrasts to P2P contrast.

For P2C contrast, we force the pixel representation to learn a more general representation with the guidance of the centroid (Wang et al. (2021); Xie et al. (2022)). Specifically, a pixel and a centroid from the same category are considered as a positive pair (v^k, c^{k+}) , while a pixel and a centroid from different categories are considered as a negative pair (v^k, c^{q-}) . We reuse the anchors in Section 3.4.4 and sample all positive and negative centroids from the centroid queue $Q_{centroid}$. Similar to P2P loss, the P2C loss is defined as:

$$\mathcal{L}_{ctr}^{P2C} = \frac{1}{\sum_{k=0}^{K-1} |V_t^k|} \sum_{k=0}^{K-1} \sum_{v_t^k \in V_t^k} \mathcal{L}_{ctr}(v_t^k, c_s^{k+}, C_s^{q-}), \quad (11)$$

where C_s^{q-} is the set of negative source centroids.

3.4.6. Centroid-to-centroid Contrast

For C2C contrast, the ideal situation is that the centroids from the same category are located near to one another, whereas centroids from other categories are located far apart. Unlike P2C contrast, the total number of centroids p ($BK \leq p \leq 2BK$) is much smaller than the pixel number in a mini-batch. Besides, calculating centroids is computationally efficient. Therefore, the centroids of the whole mini-batch can be fully involved as anchors in C2C contrast. Similar to P2P and P2C contrast, the positive pairs (c^k, c^{k+}) and negative pairs (c^k, c^{q-}) are defined according to whether centroids are from the same category. Thus, the C2C loss is defined as:

$$\mathcal{L}_{ctr}^{C2C} = \frac{1}{\sum_{k=0}^{K-1} |C_t^k|} \sum_{k=0}^{K-1} \sum_{c_t^k \in C_t^k} \mathcal{L}_{ctr}(c_t^k, c_s^{k+}, C_s^{q-}), \quad (12)$$

where C_t is the set of target centroid anchors.

Table 2: Dataset description and acquisition parameters of dataset 1 and 2.

| Subject Number | Type | Scanner | Sequence | Acquisition Parameters | | | |
|------------------|------|--------------------------------------|-------------------------------|------------------------|---------|---------|---------------------|
| | | | | TR (ms) | TE (ms) | PS (mm) | ST (mm) |
| Dataset 1 | 11 | Healthy volunteers | Philips 1.5T (Ingenia) | T1W | 5.3 | 3 | 0.36×0.36 |
| | | | | T2W | 2000 | 223 | 0.79×0.79 |
| Dataset 2 | 134 | Patients with invasive breast cancer | Philips 1.5T (Ingenia/Intera) | DCE-T1W | 6.5-7.6 | 2.9-3.5 | 0.85×0.85-0.97×0.97 |
| | | | | T2W | 2000 | 170-259 | 0.65×0.65-0.97×0.97 |

Abbreviations: TR=Repetition time; TE=Echo time; PS=Pixel spacing; ST=Slice thickness; T1W=T1-weighted; T2W=T2-weighted; DCE=Dynamic contrast-enhanced; T=Tesla.

Finally, we combine three above-mentioned contrasts (Fig. 2(d)) as our proposed multi-level semantic-guided contrastive loss:

$$\mathcal{L}_{ctr} = \mathcal{L}_{ctr}^{P2P} + \mathcal{L}_{ctr}^{P2C} + \mathcal{L}_{ctr}^{C2C}. \quad (13)$$

The overall training process of our proposed MSCDA is presented in Algorithm 1.

4. Experiments

4.1. Datasets

Dataset 1. Dataset 1 consists of test-retest breast T1-weighted (T1W) and T2-weighted (T2W) MRI images and corresponding right-breast masks of eleven healthy female volunteers, which is described in Granzier et al. (2022). The images of each subject were collected in two separate sessions (interval<7 days), during which three 3D scans were collected. Subjects were asked to lay in the prone position and remain still in the MRI scanner while both modalities are sequentially acquired. All images were acquired with an identical 1.5T MRI scanner (Philips Ingenia, Philips Healthcare, Best, the Netherlands) using a fixed clinical breast protocol without contrast. The detailed acquisition parameters are listed in Table 2. In pre-processing, we first resize all MRI slices and corresponding masks to 256×256 pixels using cubic interpolation and nearest-neighbor interpolation respectively, and then normalize images with z-score transformation. In total, dataset 1 contains 14520 (11 subjects × 2 sessions × 3 scans × 220 slices) T1W slices and 11220 (11 subjects × 2 sessions × 3 scans × 170 slices) T2W slices.

Dataset 2. Dataset 2 consists of the images from 134 subjects with histologically confirmed invasive breast cancer imaged between 2011 and 2017 in Maastricht University Medical Center+ and collected retrospectively (Granzier et al. (2020, 2021)). The images contain dynamic contrast-enhanced breast T1W and T2W MRI and corresponding right-breast masks. Similar to Dataset 1, each subject underwent the examinations with 1.5T MRI scanners (Philips Intera and Philips Ingenia (idem)) in a prone position. In particular, T1W images were acquired

before and after the intravenous injection of gadolinium-based contrast Gadobutrol (Gadovist, Bayer Healthcare, Berlin, Germany (EU)) with a volume of 15 cc and a flow rate of 2 ml/s. The acquisition parameters are also listed in Table 2. We conduct the same image pre-processing as in Dataset 1. In total, Dataset 2 contains 21793 T2W and 28540 T1W slices and they are split into three folds with 45, 45 and 44 subjects for the cross-validation depicted in Section 4.2.

4.2. Experiment Setup

As shown in Table 2, the subject population, machine vendor and acquisition parameters between the two datasets are heterogeneous, indicating the common domain shift problem in clinical practice. We set up the experiment on both Dataset 1 and 2 to transfer the knowledge of breast segmentation from healthy women to patients. In particular, the experiment consists of two scenarios: (1) Utilizing the T2W images of Dataset 1 as the source domain and the T1W images of Dataset 2 as the target domain; (2) utilizing the T1W images of Dataset 1 as the source domain and the T2W images of Dataset 2 as the target domain.

In each scenario, we establish three tasks with a different number of subjects in the source domain to validate the label-efficient learning ability of our framework. The three tasks contain four, eight and eleven (i.e., the whole dataset) randomly selected subjects respectively, and are denoted as S4, S8 and S11. To further verify the robustness of UDA performance, we split the target domain into three folds to perform a three-fold cross-validation. In each run of the cross-validation, two folds are used as the target domain for training and the remaining fold for testing.

4.3. Model Evaluation

The DSC is used as the main evaluation metric. Additionally, we use the Jaccard Similarity Coefficient (JSC) as well as precision (PRC) and sensitivity (SEN) as auxiliary evaluation metrics. These metrics are formulated as follows:

$$DSC = \frac{2 \times TP}{2 \times TP + FP + FN} \times 100\%, \quad (14)$$

Algorithm 1: MSCDA for Breast MRI

Input: Source domain image x_s and label y_s ; Target domain image x_t ;

- 1 Initialize the weights of the student network Θ_e , Θ_d with pre-trained weights, Θ_{proj} and Θ_{pred} via He et al. (2015). Initialize the teacher network by copying weights from the student network and applying stop-gradient; Initialize the memory bank Q_{pixel} and $Q_{centroid}$;
- 2 **for** $epoch = 1, E_{max}$ **do**
- 3 **foreach** *mini-batch* **do**
- 4 Apply weak and strong data augmentation;
- 5 Forward propagate weak-augmented batch in the student network to get p_s , p_t and z_t ;
- 6 Forward propagate strong-augmented batch in the teacher network to get p'_t and z'_s ;
- 7 Compute loss \mathcal{L}_{seg} using p_s and y_s via Eq.(2);
- 8 Compute loss \mathcal{L}_{con} using p_t and p'_t via Eq.(4);
- 9 Categorize the feature embedding z'_s and z_t ;
- 10 **foreach** *category* **do**
- 11 Sample pixel anchors and compute centroid anchors from z_t ;
- 12 Sample corresponding positive and negative pairs from Q_{pixel} and $Q_{centroid}$;
- 13 Update Q_{pixel} and $Q_{centroid}$ using z'_s ;
- 14 **end**
- 15 Compute loss \mathcal{L}_{ctr}^{P2P} , \mathcal{L}_{ctr}^{P2C} and \mathcal{L}_{ctr}^{C2C} via Eq.(10)-(12) respectively;
- 16 Update the student network via Eq.(4);
- 17 Update the teacher network by Eq.(5);
- 18 **end**
- 19 **end**

Output: Weights of the student network Θ_e and Θ_d .

$$JSC = \frac{TP}{TP + FP + FN} \times 100\%, \quad (15)$$

$$PRC = \frac{TP}{TP + FP} \times 100\%, \quad (16)$$

$$SEN = \frac{TP}{TP + FN} \times 100\%, \quad (17)$$

where TP, FP and FN are the number of true positive, false positive and false negative pixels of the prediction respectively. Note that we show the mean value of each metric of the three-fold cross-validation.

4.4. Implementation Details

4.4.1. Architecture

Encoder & decoder. We conduct our experiment by adopting DeepLab-v3+ (Chen et al. (2018)) with ResNet-50 (He et al. (2016)) as backbone. Benefiting from the encoder-decoder architecture, the encoder and decoder of DeepLab-v3+ are

adopted in our framework. Specifically, the hidden dimension of ResNet-50 is set to (16, 32, 64, 128), yielding a 512-dimension feature map.

Projection/Prediction Head. The projection head f_{proj} is a shallow network that contains two 1×1 convolutional layers with BatchNorm and ReLU. It projects the 512-d feature map into a 128-dimension l_2 -normalized feature embedding. The prediction head f_{pred} shares the same architecture setting with f_{proj} with the exception that the f_{pred} does not change the dimension of the features.

Memory bank. The size of the pixel queue and the centroid queue are respectively set to 32768 and 4096. In each mini-batch, we randomly sample eight pixels per category of each feature embedding to the queue and discard the oldest samples.

4.4.2. Training Settings

To accelerate the training procedure, we pre-train the DeepLab-v3+ on the source domain and then use the weights to initialize the encoder f_e and decoder f_d of our UDA framework. Additionally, the projection and prediction heads are initialized by He et al. (2015). By default, the number of pixel anchors for P2P loss is set to 32 and the number of negative pairs of (P2P, P2C, C2C) loss is set to (32768, 4096, 4096). The regularization parameters λ_1 and λ_2 are set to 1. The Adam (Kingma and Ba (2014)) optimizer is used for training the framework for $E_{max}=100$ epochs with a fixed learning rate of 0.01, batch size 24. Note that only f_e and f_d participate in inference, while f_{proj} , f_{pred} , f'_e , f'_d , f'_{proj} and $Q_{p/c}$ are discarded after training. All networks are implemented based on Python 3.8.8 and Pytorch 1.7.1 and are trained on an NVIDIA GeForce GTX 2080Ti GPU.

5. Results

5.1. Quantitative Comparison with Other Start-of-art Approaches

The performance of our proposed MSCDA is depicted in Table 3. We compared our proposed method with two state-of-art UDA approaches: CyCADA (Hoffman et al. (2018)) using adversarial learning methods and SEDA (Perone et al. (2019)) using self-training methods which are frequently used for medical images. Additionally, the two selected methods were both trained with two different domain labels, i.e. source domain labels (denoted as “Src-Only”) and target domain labels (denoted as “Supervised”). In summary, we compare MSCDA to four methods and each has two different types of backbones (U-Net (Ronneberger et al. (2015)) or DeepLab v3+ (Chen et al. (2018))), yielding eight combinations. Note that plain U-Net is not applicable for our method because the very small (e.g., 8×8) resolution in latent space leads to the inaccurate classification of embeddings.

MSCDA outperforms the other examined methods under the same task. More specifically, the DSC reaches over 83% in task S4 in both T2W-to-T1W and T1W-to-T2W scenarios (T2W-to-T1W: 87.2%, T1W-to-T2W: 83.4%), while the DSC of other

Table 3: The evaluation results of the proposed UDA framework compared with source-only, supervised training and two other UDA methods. The best performance in each metric is in bold.

| Method | Backbone | Task | Scenario 1: T2W to T1W | | | | Scenario 2: T1W to T2W | | | |
|------------|-------------|------|------------------------|-------------|-------------|-------------|------------------------|-------------|-------------|-------------|
| | | | DSC (%) | JSC (%) | PRC (%) | SEN (%) | DSC (%) | JSC (%) | PRC (%) | SEN (%) |
| Src-Only | U-Net | S11 | 65.8 | 56.7 | 70.7 | 79.8 | 74.3 | 63.7 | 88.9 | 69.3 |
| | | S8 | 64.0 | 53.9 | 82.7 | 67.8 | 74.2 | 65.1 | 87.1 | 71.9 |
| | | S4 | 21.0 | 16.0 | 96.5 | 17.4 | 60.7 | 45.2 | 96.3 | 46.0 |
| | DeepLab v3+ | S11 | 71.9 | 58.4 | 83.1 | 69.2 | 70.0 | 58.0 | 90.5 | 63.7 |
| | | S8 | 69.1 | 56.1 | 90.9 | 61.8 | 74.3 | 65.4 | 88.5 | 73.4 |
| | | S4 | 54.9 | 41.3 | 94.1 | 44.3 | 70.3 | 57.2 | 95.7 | 60.0 |
| Supervised | U-Net | - | 94.8 | 91.7 | 94.4 | 94.8 | 95.7 | 92.7 | 96.9 | 95.5 |
| | DeepLab v3+ | - | 95.8 | 92.8 | 98.0 | 94.7 | 96.0 | 93.0 | 96.2 | 96.5 |
| CyCADA | U-Net | S11 | 78.7 | 68.8 | 86.9 | 79.4 | 79.7 | 69.3 | 90.5 | 75.6 |
| | | S8 | 77.0 | 66.4 | 83.5 | 79.8 | 78.5 | 66.8 | 91.5 | 72.1 |
| | | S4 | 54.5 | 42.6 | 94.7 | 45.1 | 63.0 | 49.7 | 97.8 | 50.7 |
| | DeepLab v3+ | S11 | 80.0 | 68.0 | 78.6 | 86.0 | 73.8 | 61.3 | 85.8 | 70.6 |
| | | S8 | 77.2 | 64.5 | 81.1 | 79.2 | 70.3 | 59.0 | 92.1 | 64.5 |
| | | S4 | 64.0 | 50.4 | 92.4 | 54.1 | 67.6 | 53.8 | 92.8 | 57.4 |
| SEDA | U-Net | S11 | 79.0 | 67.1 | 81.4 | 82.6 | 81.2 | 70.4 | 96.2 | 72.7 |
| | | S8 | 79.4 | 70.0 | 83.3 | 84.3 | 80.2 | 70.3 | 92.0 | 75.0 |
| | | S4 | 69.0 | 56.1 | 93.4 | 60.0 | 73.5 | 60.8 | 98.9 | 61.3 |
| | DeepLab v3+ | S11 | 81.7 | 70.6 | 88.6 | 79.2 | 82.5 | 73.7 | 94.0 | 78.5 |
| | | S8 | 80.3 | 68.4 | 88.0 | 77.9 | 82.4 | 71.4 | 83.9 | 83.2 |
| | | S4 | 71.4 | 57.9 | 95.4 | 60.1 | 75.5 | 62.5 | 98.5 | 63.5 |
| MSCDA | DeepLab v3+ | S11 | 88.6 | 79.9 | 86.5 | 92.3 | 83.1 | 71.8 | 88.7 | 79.5 |
| | | S8 | 89.2 | 81.0 | 89.3 | 89.9 | 84.0 | 73.2 | 91.7 | 78.8 |
| | | S4 | 87.2 | 78.0 | 92.4 | 83.6 | 83.4 | 72.5 | 98.0 | 73.8 |

methods are below 76% (e.g., CyCADA, T2W-to-T1W: 64.0%, T1W-to-T2W: 67.6%; SEDA, T2W-to-T1W: 71.4%, T1W-to-T2W: 75.5%). This result is supported by other evaluation metrics, such as JSC and SEN. As it can be seen in the bottom of Table 3, in both scenarios, MSCDA achieved better results in all evaluated metrics except in PRC although it reaches over 92%. For the other two tasks (S8 and S11), the proposed method in general outperforms other approaches. The box plot (see Fig. 3) also indicates that MSCDA method not only performs better but also has a smaller interquartile range than Src-Only and the other two methods. The segmentation results of MSCDA and other methods are shown in Fig. 4.

From Table 3, one can observe that when comparing the performance between different tasks (i.e., S11, S8 and S4), MSCDA shows high label-efficient learning ability. More precisely, the DSC of our methods in T2W-to-T1W scenarios only drops 2.0% from 89.2% to 87.2% while CyCACA and SEDA drop 16.0% and 10.3% respectively; The DSC of our method in T1W-to-T2W scenario remains relatively stable across three tasks with the difference of 0.9% across tasks. Compared to our model, the performance of other methods drops significantly as the number of the source subjects decreases. Therefore, the obtained results show that our method is less sensitive to the size of source domain compared to other UDA methods. Notably, the performance of our method is very close to that of supervised learning (MSCDA: DSC=89.2%, JSC=81.0%, PRC=89.3% SEN=89.9%; Supervised: DSC=95.8%, JSC=92.8%, PRC=98.0%, SEN=94.7%) when training with the eight source subjects (task S8) in T2W-to-T1W scenario, demonstrating the potential of contrastive representation learning and self-training framework.

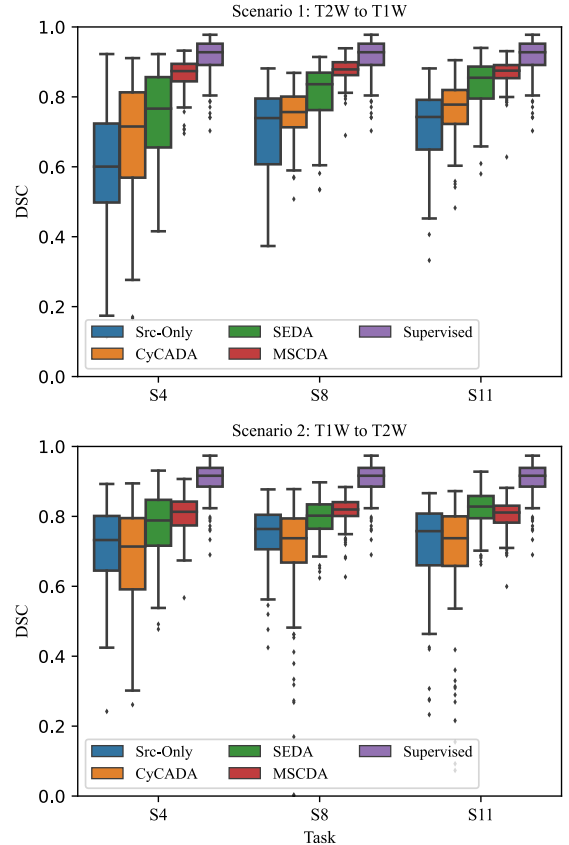


Figure 3: The box plot comparison of the DSC between our proposed MSCDA and other methods. All methods are equipped with DeepLab v3+ as the backbone. The plots show the distribution of model performance at a subject level. The DSC of each subject is the mean value of all slices containing foreground pixels.

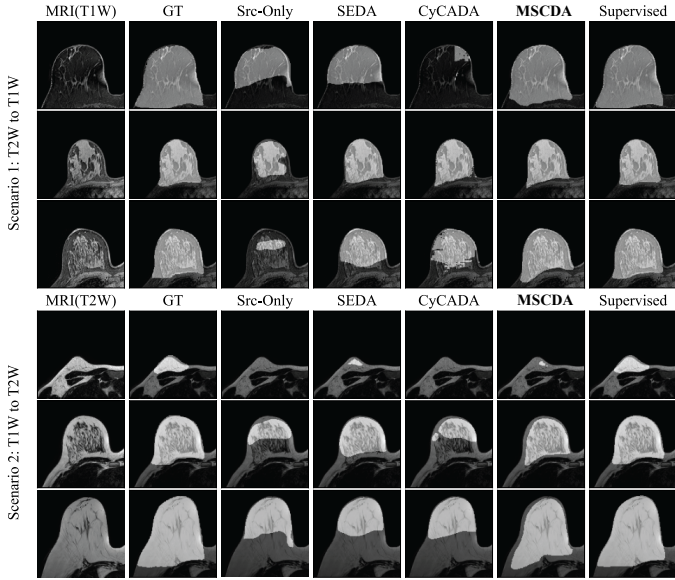


Figure 4: Segmentation results compared with previous methods on scenario 1/2 task S4. All methods are equipped with DeepLab v3+ as the backbone. In each scenario, the subplots from left to right indicate the original image, ground truth, Src-Only, SEDA, CyCADA, our proposed MSCDA and supervised training respectively.

5.2. Ablation Study of Different Loss Function & Augmentation

In order to investigate the contribution of augmentation and different loss function, we conduct an ablation experiment by removing/adding each component separately. We test the network on scenario 1 task S4 fold 1 with combinations of self-training, data augmentation, P2P, P2C and C2C contrast. All the networks are trained under the same experimental settings as Section 4.4. As illustrated in Table 4, adding data augmentation (see case 2) to self-training can increase the DSC by 21.3% compared to plain self-training (see case 1). Combining case 2 with P2P (see case 3) or P2C (see case 4) contrast increase the DSC to 80.2% and 76.0% respectively. However, when adding C2C contrast into case 2 (see case 5), the network performance deteriorates to a DSC of 67.3%, indicating centroid-level contrastive learning does not benefit feature embeddings in our breast segmentation task. Nonetheless, this shortcoming is canceled out by adding P2P or P2C contrast, as shown in case 6 and 8. When integrating all contrasts together (see case 9), the DSC reaches highest score of 82.2%, an increment of 31.9% compared to the simple case 1. In summary, these results suggest that our proposed contrastive loss can improve the self-training framework to achieve promising segmentation performance.

5.3. Ablation Study of Contrast Between Domains

As mentioned in Section 3.4, we compute three types of contrasts between the student and teacher networks. In particular, only the **target** feature embeddings in the **student** network are sampled as anchors, while only the **source** feature embeddings in the **teacher** network are sampled to update the memory bank. To further elaborate our selection, we conduct an additional, complementary ablation study by selecting different domains

Table 4: Ablation study of each proposed component on scenario 1 task S4 fold 1. A check mark indicates that a specific component is applied. The DSC is utilized to evaluate the performance and the extra points gained compared to the baseline (case 1) are listed.

| case | Self-training | Aug. | P2P | P2C | C2C | DSC (%) | gain (%) |
|------|---------------|------|-----|-----|-----|-------------|--------------|
| 1 | ✓ | | | | | 50.3 | |
| 2 | ✓ | | ✓ | | | 71.6 | +21.3 |
| 3 | ✓ | | ✓ | ✓ | | 80.2 | +29.9 |
| 4 | ✓ | | ✓ | | ✓ | 76.0 | +25.7 |
| 5 | ✓ | | ✓ | | | 67.3 | +17.0 |
| 6 | ✓ | | ✓ | ✓ | ✓ | 79.1 | +28.8 |
| 7 | ✓ | | ✓ | ✓ | ✓ | 81.6 | +31.3 |
| 8 | ✓ | | ✓ | ✓ | ✓ | 81.5 | +31.2 |
| 9 | ✓ | | ✓ | ✓ | ✓ | 82.2 | +31.9 |

Table 5: Ablation study of contrast between domains on scenario 1 task S4 fold 1. A check mark indicates that a specific component is applied. The DSC is utilized to evaluate the performance and the extra points gained compared to the lowest value (case 1) are listed. The best performed combination is in bold.

| case | Student Network (anchor) | | Teacher Network (queue) | | DSC (%) | gain (%) |
|------|--------------------------|--------|-------------------------|--------|-------------|-------------|
| | Source | Target | Source | Target | | |
| 1 | ✓ | ✓ | ✓ | ✓ | 77.0 | +0.5 |
| 2 | ✓ | ✓ | ✓ | | 76.5 | |
| 3 | ✓ | ✓ | | ✓ | 77.5 | +1.0 |
| 4 | ✓ | | ✓ | ✓ | 78.1 | +1.6 |
| 5 | | ✓ | ✓ | ✓ | 82.0 | +5.5 |
| 6 | ✓ | ✓ | | ✓ | 78.7 | +2.2 |
| 7 | | ✓ | ✓ | | 82.2 | +5.7 |

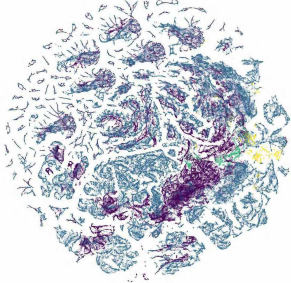
for computing contrast. Note that all other experimental settings remained unchanged.

As shown in Table 5, we observe that the best candidate (see case 7, DSC=82.2%) is the combination of the target samples in the student network and the source sample in the teacher network. More specifically, we adopt **source** samples from the teacher network to create the memory bank and to guide the **target** samples from the student network. As expected, when adding target samples to the memory bank (see case 5), the performance shows a minor decrease of 0.2%, indicating that the pseudo label brings uncertainty to the model. It is worth noticing that we observe 5.7% of degradation when adopting additional source samples as anchor (see case 2). It might be due to the overfitting of the model on the source domain.

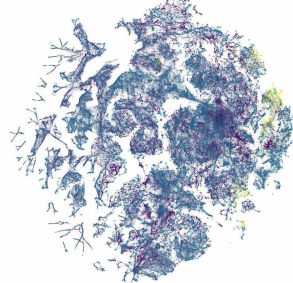
5.4. Visualization of Feature Maps

To visualize the effect of our proposed method on domain shift, we plot the learned features from the source and target testing images with t-SNE (Van der Maaten and Hinton (2008)). The learned features are obtained by using DeepLab v3+ (Chen et al. (2018)) as the backbone. At the pixel level (Fig. 5), when no domain adaptation method is applied, the breast pixels of Src-Only highly overlap with non-breast pixels (Fig. 5(a)), making them indistinguishable. Compared to Src-Only, the

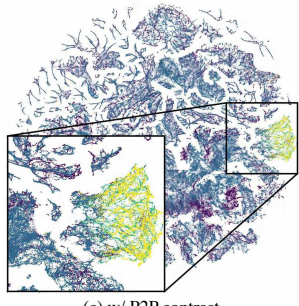
● NonBreast-Source ● NonBreast-Target ● Breast-Source ● Breast-Target



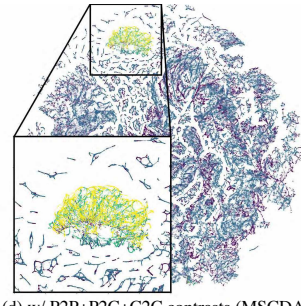
(a) Src-Only



(b) w/o contrast (self-training)



(c) w/ P2P contrast



(d) w/ P2P+P2C+C2C contrasts (MSCDA)

Figure 5: t-SNE visualization of the pixel representations on scenario 1 task S4. Each colored point indicates a categorized pixel representation in the high dimension feature map. Note that we only partially visualize the testing images of the target domain due to the large dataset size. All methods are equipped with DeepLab v3+ as the backbone.

self-training (Fig. 5(b)) makes it possible to align part of the breast pixels between domains but fails to separate them from non-breast pixels. Incorporating P2P contrast (Fig. 5(c)) highly aligns the breast pixels; however, a number of breast pixels are contaminated by non-breast pixels which may increase the error. In contrast to the above-mentioned methods, our method nicely aligns the breast pixels and separates them from non-breast pixels.

The visualization of the centroid level (Fig. 6) further illustrates the effect of our method on the feature space. Compared to the pixel level, the uneven distribution caused by the imbalanced dataset is alleviated at the centroid level, making the visualization clearer. We can observe that the learned centroids of different categories in all methods are linearly separable. Before self-training, the centroids of the same category are completely separable by domain, as can be observed in Fig. 6(a). When self-training is applied (Fig. 6(b)), the non-breast centroids are clustered together while the breast centroids are still not aligned. The P2P contrast (Fig. 6(c)) improves the centroid alignment between domains but is still not fully overlapped. In our method (Fig. 6(d)), the centroids of the same category share a well-aligned tight representation space. In summary, the t-SNE visualization demonstrates the effect of domain shift in the feature space, an effect that can be mitigated by applying our method.

● NonBreast-Source ● NonBreast-Target ● Breast-Source ● Breast-Target



(a) Src-Only



(b) w/o contrast (self-training)



(c) w/ P2P contrast



(d) w/ P2P+P2C+C2C contrasts (MSCDA)

Figure 6: t-SNE visualization of the centroid representations on scenario 1 task S4. Each colored point indicates a categorized centroid representation in the high dimension feature map. All testing images of the target domain are included in the visualization. All methods are equipped with DeepLab v3+ as the backbone.

6. Conclusion

In this paper, a novel multi-level semantic-guided contrastive UDA framework for breast MRI segmentation, named MSCDA, is introduced. We found that by combining self-training with multi-level contrastive loss, the semantic information can be further exploited to improve segmentation performance on the unlabeled target domain. Furthermore, we built a hybrid memory bank for sample storage and proposed a category-wise cross-domain sampling strategy to balance the contrastive pairs. The proposed model shows a robust and clinically relevant performance in a cross-sequence label-sparse scenario of breast MRI segmentation. The code of our MSCDA model is available at <https://github.com/ShengKuangCN/MSCDA>.

Acknowledgements

The authors disclosed receipt of the following financial support for the research, authorship, and/or publication of this article: Authors acknowledge financial support from ERC advanced grant (ERC-ADG-2015 n° 694812 - Hypoximmuno), ERC-2020-PoC: 957565-AUTO.DISTINCT. Authors also acknowledge financial support from the European Union's Horizon 2020 research and innovation programme under grant agreement: ImmunoSABR n° 733008, CHAMELEON n° 952172, EuCanImage n° 952103. This work was also partially supported by the Dutch Cancer Society (KWF Kankerbestrijding), project number 14449.

References

Antonelli, M., Reinke, A., Bakas, S., Farahani, K., Kopp-Schneider, A., Landman, B.A., Litjens, G., Menze, B., Ronneberger, O., Summers, R.M., et al., 2022. The medical segmentation decathlon. *Nature Communications* 13, 1–13.

Azamjah, N., Soltan-Zadeh, Y., Zayeri, F., 2019. Global trend of breast cancer mortality rate: a 25-year study. *Asian Pacific journal of cancer prevention: APJCP* 20, 2015.

Bernard, O., Lalande, A., Zotti, C., Cervenansky, F., Yang, X., Heng, P.A., Cetin, I., Lekadir, K., Camara, O., Ballester, M.A.G., et al., 2018. Deep learning techniques for automatic mri cardiac multi-structures segmentation and diagnosis: is the problem solved? *IEEE transactions on medical imaging* 37, 2514–2525.

Bishop, C.M., Nasrabadi, N.M., 2006. Pattern recognition and machine learning, volume 4. Springer.

Chaitanya, K., Erdil, E., Karani, N., Konukoglu, E., 2020. Contrastive learning of global and local features for medical image segmentation with limited annotations. *Advances in Neural Information Processing Systems* 33, 12546–12558.

Chen, C., Dou, Q., Chen, H., Qin, J., Heng, P.A., 2019a. Synergistic image and feature adaptation: Towards cross-modality domain adaptation for medical image segmentation, in: *Proceedings of the AAAI conference on artificial intelligence*, pp. 865–872.

Chen, C., Xie, W., Huang, W., Rong, Y., Ding, X., Huang, Y., Xu, T., Huang, J., 2019b. Progressive feature alignment for unsupervised domain adaptation, in: *Proceedings of the IEEE/CVF conference on computer vision and pattern recognition*, pp. 627–636.

Chen, L.C., Zhu, Y., Papandreou, G., Schroff, F., Adam, H., 2018. Encoder-decoder with atrous separable convolution for semantic image segmentation, in: *Proceedings of the European conference on computer vision (ECCV)*, pp. 801–818.

Chen, T., Kornblith, S., Norouzi, M., Hinton, G., 2020a. A simple framework for contrastive learning of visual representations, in: *International conference on machine learning*, PMLR, pp. 1597–1607.

Chen, X., Fan, H., Girshick, R., He, K., 2020b. Improved baselines with momentum contrastive learning. *arXiv preprint arXiv:2003.04297*.

Dalmaş, M.U., Litjens, G., Holland, K., Setio, A., Mann, R., Karssemeijer, N., Gubern-Mérida, A., 2017. Using deep learning to segment breast and fibroglandular tissue in mri volumes. *Medical physics* 44, 533–546.

Deng, J., Dong, W., Socher, R., Li, L.J., Li, K., Fei-Fei, L., 2009. Imagenet: A large-scale hierarchical image database, in: *2009 IEEE conference on computer vision and pattern recognition*, Ieee, pp. 248–255.

Dou, Q., Ouyang, C., Chen, C., Chen, H., Glocker, B., Zhuang, X., Heng, P.A., 2018. Pnp-adanet: Plug-and-play adversarial domain adaptation network with a benchmark at cross-modality cardiac segmentation. *arXiv preprint arXiv:1812.07907*.

El Adoui, M., Mahmoudi, S.A., Larhman, M.A., Benjelloun, M., 2019. Mri breast tumor segmentation using different encoder and decoder cnn architectures. *Computers* 8, 52.

Francies, F.Z., Hull, R., Khanyile, R., Dlamini, Z., 2020. Breast cancer in low-middle income countries: Abnormality in splicing and lack of targeted treatment options. *American Journal of Cancer Research* 10, 1568.

Gallego-Ortiz, C., Martel, A.L., 2017. Using quantitative features extracted from t2-weighted mri to improve breast mri computer-aided diagnosis (cad). *PloS one* 12, e0187501.

Goodfellow, I., Pouget-Abadie, J., Mirza, M., Xu, B., Warde-Farley, D., Ozair, S., Courville, A., Bengio, Y., 2014. Generative adversarial nets. *Advances in neural information processing systems* 27.

Granzier, R., Ibrahim, A., Primakov, S., Keek, S., Halilaj, I., Zwanenburg, A., Engelen, S., Lobbes, M., Lambin, P., Woodruff, H., et al., 2022. Test-retest data for the assessment of breast mri radiomic feature repeatability. *Journal of Magnetic Resonance Imaging* 56, 592–604.

Granzier, R., Verbakel, N., Ibrahim, A., Van Timmeren, J., Van Nijnatten, T., Leijenaar, R., Lobbes, M., Smidt, M., Woodruff, H., 2020. Mri-based radiomics in breast cancer: Feature robustness with respect to inter-observer segmentation variability. *Scientific reports* 10, 1–11.

Granzier, R.W., Ibrahim, A., Primakov, S.P., Samiei, S., van Nijnatten, T.J., de Boer, M., Heuts, E.M., Hulsmans, F.J., Chatterjee, A., Lambin, P., et al., 2021. Mri-based radiomics analysis for the pretreatment prediction of pathologic complete tumor response to neoadjuvant systemic therapy in breast cancer patients: a multicenter study. *Cancers* 13, 2447.

Grill, J.B., Strub, F., Alché, F., Tallec, C., Richemond, P., Buchatskaya, E., Doersch, C., Avila Pires, B., Guo, Z., Gheshlaghi Azar, M., et al., 2020. Bootstrap your own latent-a new approach to self-supervised learning. *Advances in neural information processing systems* 33, 21271–21284.

Guan, H., Liu, M., 2021. Domain adaptation for medical image analysis: a survey. *IEEE Transactions on Biomedical Engineering* 69, 1173–1185.

Gupta, D., Billadello, L., 2017. Breast mr imaging in newly diagnosed breast cancer. *Radiologic Clinics* 55, 541–552.

He, J., Deng, Z., Qiao, Y., 2019. Dynamic multi-scale filters for semantic segmentation, in: *Proceedings of the IEEE/CVF International Conference on Computer Vision*, pp. 3562–3572.

He, K., Fan, H., Wu, Y., Xie, S., Girshick, R., 2020. Momentum contrast for unsupervised visual representation learning, in: *Proceedings of the IEEE/CVF conference on computer vision and pattern recognition*, pp. 9729–9738.

He, K., Zhang, X., Ren, S., Sun, J., 2015. Delving deep into rectifiers: Surpassing human-level performance on imagenet classification, in: *Proceedings of the IEEE international conference on computer vision*, pp. 1026–1034.

He, K., Zhang, X., Ren, S., Sun, J., 2016. Deep residual learning for image recognition, in: *Proceedings of the IEEE conference on computer vision and pattern recognition*, pp. 770–778.

Hoffman, J., Tzeng, E., Park, T., Zhu, J.Y., Isola, P., Saenko, K., Efros, A., Darrell, T., 2018. Cycada: Cycle-consistent adversarial domain adaptation, in: *International conference on machine learning*, Pmlr, pp. 1989–1998.

Hoffman, J., Wang, D., Yu, F., Darrell, T., 2016. Fcns in the wild: Pixel-level adversarial and constraint-based adaptation. *arXiv preprint arXiv:1612.02649*.

Hoyer, L., Dai, D., Van Gool, L., 2022. Daformer: Improving network architectures and training strategies for domain-adaptive semantic segmentation, in: *Proceedings of the IEEE/CVF Conference on Computer Vision and Pattern Recognition*, pp. 9924–9935.

Hu, B., Xu, K., Zhang, Z., Chai, R., Li, S., Zhang, L., 2018. A radiomic nomogram based on an apparent diffusion coefficient map for differential diagnosis of suspicious breast findings. *Chinese Journal of Cancer Research* 30, 432.

Hu, X., Zeng, D., Xu, X., Shi, Y., 2021. Semi-supervised contrastive learning for label-efficient medical image segmentation, in: *International Conference on Medical Image Computing and Computer-Assisted Intervention*, Springer, pp. 481–490.

Isensee, F., Petersen, J., Klein, A., Zimmerer, D., Jaeger, P.F., Kohl, S., Wasserthal, J., Koehler, G., Norajitra, T., Wirkert, S., et al., 2018. nnunet: Self-adapting framework for u-net-based medical image segmentation. *arXiv preprint arXiv:1809.10486*.

Ivanovska, T., Jentschke, T.G., Daboul, A., Hegenscheid, K., Völzke, H., Wörgötter, F., 2019. A deep learning framework for efficient analysis of breast volume and fibroglandular tissue using mr data with strong artifacts. *International journal of computer assisted radiology and surgery* 14, 1627–1633.

Jiang, J., Hu, Y.C., Tyagi, N., Zhang, P., Rimmer, A., Mageras, G.S., Deasy, J.O., Veeraraghavan, H., 2018. Tumor-aware, adversarial domain adaptation from ct to mri for lung cancer segmentation, in: *International conference on medical image computing and computer-assisted intervention*, Springer, pp. 777–785.

Kim, T., Cha, M., Kim, H., Lee, J.K., Kim, J., 2017. Learning to discover cross-domain relations with generative adversarial networks, in: *International conference on machine learning*, PMLR, pp. 1857–1865.

Kingma, D.P., Ba, J., 2014. Adam: A method for stochastic optimization. *arXiv preprint arXiv:1412.6980*.

Kouw, W.M., Loog, M., 2018. An introduction to domain adaptation and transfer learning. *arXiv preprint arXiv:1812.11806*.

Liu, Z., Zhu, Z., Zheng, S., Liu, Y., Zhou, J., Zhao, Y., 2022. Margin preserving self-paced contrastive learning towards domain adaptation for medical image segmentation. *IEEE Journal of Biomedical and Health Informatics* 26, 638–647.

Long, J., Shelhamer, E., Darrell, T., 2015. Fully convolutional networks for semantic segmentation, in: *Proceedings of the IEEE conference on computer vision and pattern recognition*, pp. 3431–3440.

Van der Maaten, L., Hinton, G., 2008. Visualizing data using t-sne. *Journal of machine learning research* 9.

Mehrkanoon, S., 2019. Cross-domain neural-kernel networks. *Pattern Recognition Letters* 125, 474–480.

Mehrkanoon, S., Suykens, J.A.K., 2017. Regularized semipaired kernel CCA

for domain adaptation. *IEEE transactions on neural networks and learning systems* 29, 3199–3213.

Negi, A., Raj, A.N.J., Nersisson, R., Zhuang, Z., Murugappan, M., 2020. Rda-unet-wgan: an accurate breast ultrasound lesion segmentation using wasserstein generative adversarial networks. *Arabian Journal for Science and Engineering* 45, 6399–6410.

Oord, A.v.d., Li, Y., Vinyals, O., 2018. Representation learning with contrastive predictive coding. *arXiv preprint arXiv:1807.03748* .

Perone, C.S., Ballester, P., Barros, R.C., Cohen-Adad, J., 2019. Unsupervised domain adaptation for medical imaging segmentation with self-ensembling. *NeuroImage* 194, 1–11.

Perone, C.S., Cohen-Adad, J., 2018. Deep semi-supervised segmentation with weight-averaged consistency targets, in: *Deep learning in medical image analysis and multimodal learning for clinical decision support*. Springer, pp. 12–19.

Piantadosi, G., Sansone, M., Sansone, C., 2018. Breast segmentation in mri via u-net deep convolutional neural networks, in: *2018 24th international conference on pattern recognition (ICPR)*, IEEE. pp. 3917–3922.

Ronneberger, O., Fischer, P., Brox, T., 2015. U-net: Convolutional networks for biomedical image segmentation, in: *International Conference on Medical image computing and computer-assisted intervention*, Springer. pp. 234–241.

Saslow, D., Boetes, C., Burke, W., Harms, S., Leach, M.O., Lehman, C.D., Morris, E., Pisano, E., Schnall, M., Sener, S., et al., 2007. American cancer society guidelines for breast screening with mri as an adjunct to mammography. *CA: a cancer journal for clinicians* 57, 75–89.

Shanis, Z., Gerber, S., Gao, M., Enquobahrie, A., 2019. Intramodality domain adaptation using self ensembling and adversarial training, in: *Domain Adaptation and Representation Transfer and Medical Image Learning with Less Labels and Imperfect Data*. Springer, pp. 28–36.

Sudre, C.H., Li, W., Vercauteren, T., Ourselin, S., Jorge Cardoso, M., 2017. Generalised dice overlap as a deep learning loss function for highly unbalanced segmentations, in: *Deep learning in medical image analysis and multimodal learning for clinical decision support*. Springer, pp. 240–248.

Sung, H., Ferlay, J., Siegel, R.L., Laversanne, M., Soerjomataram, I., Jemal, A., Bray, F., 2021. Global cancer statistics 2020: Globocan estimates of incidence and mortality worldwide for 36 cancers in 185 countries. *CA: a cancer journal for clinicians* 71, 209–249.

Tarvainen, A., Valpola, H., 2017. Mean teachers are better role models: Weight-averaged consistency targets improve semi-supervised deep learning results. *Advances in neural information processing systems* 30.

Tsai, Y.H., Hung, W.C., Schulter, S., Sohn, K., Yang, M.H., Chandraker, M., 2018. Learning to adapt structured output space for semantic segmentation, in: *Proceedings of the IEEE conference on computer vision and pattern recognition*, pp. 7472–7481.

Tzeng, E., Hoffman, J., Saenko, K., Darrell, T., 2017. Adversarial discriminative domain adaptation, in: *Proceedings of the IEEE conference on computer vision and pattern recognition*, pp. 7167–7176.

Vu, T.H., Jain, H., Bucher, M., Cord, M., Pérez, P., 2019. Advent: Adversarial entropy minimization for domain adaptation in semantic segmentation, in: *Proceedings of the IEEE/CVF Conference on Computer Vision and Pattern Recognition*, pp. 2517–2526.

Wang, W., Zhou, T., Yu, F., Dai, J., Konukoglu, E., Van Gool, L., 2021. Exploring cross-image pixel contrast for semantic segmentation, in: *Proceedings of the IEEE/CVF International Conference on Computer Vision*, pp. 7303–7313.

Wu, H., Zhang, J., Huang, K., Liang, K., Yu, Y., 2019. Fastfcn: Rethinking dilated convolution in the backbone for semantic segmentation. *arXiv preprint arXiv:1903.11816* .

Wu, S., Weinstein, S.P., Conant, E.F., Kontos, D., 2013. Automated fibroglandular tissue segmentation and volumetric density estimation in breast mri using an atlas-aided fuzzy c-means method. *Medical physics* 40, 122302.

Wu, Z., Xiong, Y., Yu, S.X., Lin, D., 2018. Unsupervised feature learning via non-parametric instance discrimination, in: *Proceedings of the IEEE conference on computer vision and pattern recognition*, pp. 3733–3742.

Xie, B., Li, S., Li, M., Liu, C.H., Huang, G., Wang, G., 2022. Sepico: Semantic-guided pixel contrast for domain adaptive semantic segmentation. *arXiv preprint arXiv:2204.08808* .

Yi, Z., Zhang, H., Tan, P., Gong, M., 2017. Dualgan: Unsupervised dual learning for image-to-image translation, in: *Proceedings of the IEEE international conference on computer vision*, pp. 2849–2857.

Zhang, F., Koltun, V., Torr, P., Ranftl, R., Richter, S.R., 2022. Unsupervised contrastive domain adaptation for semantic segmentation. *arXiv preprint arXiv:2204.08399* .

Zhang, H., Dana, K., Shi, J., Zhang, Z., Wang, X., Tyagi, A., Agrawal, A., 2018a. Context encoding for semantic segmentation, in: *The IEEE Conference on Computer Vision and Pattern Recognition (CVPR)*.

Zhang, J., Saha, A., Zhu, Z., Mazurowski, M.A., 2018b. Hierarchical convolutional neural networks for segmentation of breast tumors in mri with application to radiogenomics. *IEEE transactions on medical imaging* 38, 435–447.

Zhang, J., Saha, A., Zhu, Z., Mazurowski, M.A., 2018c. Hierarchical convolutional neural networks for segmentation of breast tumors in mri with application to radiogenomics. *IEEE transactions on medical imaging* 38, 435–447.

Zhang, L., Mohamed, A.A., Chai, R., Guo, Y., Zheng, B., Wu, S., 2020. Automated deep learning method for whole-breast segmentation in diffusion-weighted breast mri. *Journal of Magnetic Resonance Imaging* 51, 635–643.

Zhang, P., Zhang, B., Zhang, T., Chen, D., Wang, Y., Wen, F., 2021. Prototypical pseudo label denoising and target structure learning for domain adaptive semantic segmentation, in: *Proceedings of the IEEE/CVF conference on computer vision and pattern recognition*, pp. 12414–12424.

Zhang, Y., Chen, J.H., Chang, K.T., Park, V.Y., Kim, M.J., Chan, S., Chang, P., Chow, D., Luk, A., Kwong, T., et al., 2019. Automatic breast and fibroglandular tissue segmentation in breast mri using deep learning by a fully-convolutional residual neural network u-net. *Academic radiology* 26, 1526–1535.

Zhang, Y., Miao, S., Mansi, T., Liao, R., 2018d. Task driven generative modeling for unsupervised domain adaptation: Application to x-ray image segmentation, in: *International Conference on Medical Image Computing and Computer-Assisted Intervention*, Springer. pp. 599–607.

Zhao, X., Vemulapalli, R., Mansfield, P.A., Gong, B., Green, B., Shapira, L., Wu, Y., 2021a. Contrastive learning for label efficient semantic segmentation, in: *Proceedings of the IEEE/CVF International Conference on Computer Vision*, pp. 10623–10633.

Zhao, Z., Xu, K., Li, S., Zeng, Z., Guan, C., 2021b. Mt-uda: Towards unsupervised cross-modality medical image segmentation with limited source labels, in: *International Conference on Medical Image Computing and Computer-Assisted Intervention*, Springer. pp. 293–303.

Zhong, Y., Yuan, B., Wu, H., Yuan, Z., Peng, J., Wang, Y.X., 2021. Pixel contrastive-consistent semi-supervised semantic segmentation, in: *Proceedings of the IEEE/CVF International Conference on Computer Vision*, pp. 7273–7282.

Zhu, J.Y., Park, T., Isola, P., Efros, A.A., 2017. Unpaired image-to-image translation using cycle-consistent adversarial networks, in: *Proceedings of the IEEE international conference on computer vision*, pp. 2223–2232.

Zhuang, X., Shen, J., 2016. Multi-scale patch and multi-modality atlases for whole heart segmentation of mri. *Medical image analysis* 31, 77–87.